N_8^- Polynitrogen Stabilized on Boron Doped Graphene as Metal-free Electrocatalysts for Oxygen Reduction Reaction

Zhenhua Yao [1,2,#], Maocong Hu [1,2,#], Zafar Iqbal [1], Xianqin Wang [1,*]

[1]Department of Chemical and Materials Engineering, New Jersey Institute of Technology, Newark, New Jersey 07102, USA

[2] Current address: Key Laboratory of Optoelectronic Chemical Materials and Devices, Ministry of Education, School of Chemical and Environmental Engineering, Jianghan University, Wuhan 430056, P. R. China

Abstract: Polynitrogen (PN) chain was predicted theoretically to be stable at ambient pressure by intercalating in multiple graphene layers. In this work, polynitrogen (N_8^-) deposited on boron-doped graphene (PN-BG) and graphene (PN-G) was synthesized experimentally by a facile cyclic voltammetry (CV) method. It was further used for oxygen reduction reaction (ORR), which showed superior activity via a four-electron pathway mechanism. BG was prepared by a one-pot hydrothermal method. Characterizations over BG substrate, including X-ray photoelectron spectroscopy (XPS), Raman, Brunauer-Emmett-Teller (BET), scanning electron microscope (SEM), and transmission electron microscopy (TEM), demonstrated that boron atoms were successfully doped into graphene matrix. The formation of polynitrogen (N_8^-) on BG were confirmed by attenuated total reflection Fourier transform infrared spectroscopy (ATR-FTIR) and temperature-programmed desorption (TPD). A larger amount of N_8^- was obtained on boron-doped graphene than that on graphene. Rotating disk electrode (RDE) measurements indicated that PN-BG showed higher current density than PN-G catalyst due to the larger amount of N_8^- on BG. Compared to commercial Pt/C catalyst, PN-B1G has much better methanol tolerance. Kinetic study was further carried to investigate the ORR pathway. Natural bonding orbital (NBO) analysis confirmed the mechanism. This work provides a facile strategy to modify graphene structure and efficiently stabilize N_8^- on graphene based matrix.

Keywords: Polynitrogen, boron, doped graphene, metal free catalyst, oxygen reduction reaction

1. Introduction

Polynitrogen compounds have attracted considerable attention due to their potential use as a high-energy density material (HEDMs) while decomposing into an inert gas, N_2, that is friendly to the environment with a large amount of energy released[1-3]. Although many possible stable structures have been predicted by calculations [4], few reports on experimental detection of PN have been published. They are either short-lived or synthesized under harsh conditions [5-7]. Abou-Rachid et al. theoretically demonstrated that a polymeric nitrogen chain N_8 could be encapsulated in a carbon nanotube under ambient conditions by a charge transfer interactions between nitrogen chain and carbon nanotube [8, 9]. In addition, Hirshberg et al. used electronic structure calculations predicting a stable molecular crystalline of N_8 that is more stable than other N_n polynitrogen species [10]. Later on, for the first time, our group experimentally synthesized N_8^- polynitrogen phase (PN) stabilized on positively charged sidewalls of multi-walled carbon nanotube (MWNT) under ambient condition using cyclic voltammetry (CV) approach, which confirmed the calculated results. The synthesized PN was further used as catalyst for oxygen reduction reaction (ORR), which demonstrated superior activity [11]. Most recently, ab initio DFT calculations indicate that polynitrogen would be also confined in boron nitride nanotube BNNT(5,5), a multilayer BN matrix, and graphene sheets at ambient conditions, owing to the charge transfer from hosting materials to polymeric nitrogen [12-14]. Similar simulation results were also reported by Abou-Rachid et al., where polynitrogen chains N_8 could be intercalated in multiple graphene layers and remained stable at ambient pressure. Since graphite structure does not involve geometric parameters, such as radius and chirality in carbon nanotubes, graphene based matrix may be a promising support to stabilize the polynitrogen by charge transfer from graphene matrix to nitrogen chain [15]. It inspires us to

synthesize polynitrogen N_8 (PN) on graphene based matrix at ambient conditions with cyclic voltammetry (CV) approach.

Graphene, as a two dimensional graphitic material, will facilitate electron transport, and make it an attractive support for electrochemical applications [16-20]. Especially, heteroatom doping would modify surface structure and electronic properties, which will directly enhance its electrocatalytic activity and stability of catalyst nanoparticles [21-26]. Boron atoms, possessing a similar atomic size as carbon and three valence electrons for binding with carbon atoms, could be introduced into the carbon lattice by substitutional doping [22, 23, 27]. In B-doped graphene, electron transfer happened from boron to carbon due to the lower electronegativity of B (2.04) than C (2.55). This will result into a generation of partial positive charge on B atom and lead to more facile electron transfer, which will become the active centers for the stabilization of polynitrogen N_8^- (PN) chain [11].

In this work, polynitrogen N_8^- deposited on graphene (PN-G), boron-doped graphene (PN-BG) were harvested using cyclic voltammetry (CV) method. Graphene and boron doped graphene with tunable boron content of 1.23-2.78 atom% were used as the substrates, which were prepared by a facile hydrothermal method. The PN samples were further tested as cathode catalysts for oxygen reduction reaction (ORR) in alkaline solution. The optimal PN-BG catalyst showed high activity via a four-electron pathway, making it a promising candidate as ORR electrode material.

2. Experimental section

2.1.1 Preparation of graphene and boron-doped graphene. Graphite oxide was synthesized from graphite powder following a modified Hummers method according to

previously reported work [28]. Then it was dispersed into deionized water and sonicated for 30 min to exfoliate oxidized graphite particles to graphene oxide (GO) colloid solution.

Boron-doped graphene (BG) was synthesized via hydrothermal method in the presence of $NaBH_4$ [29]. Briefly, a 20 mL of $NaBH_4$ aqueous was gradually added into the 100 mL of prepared GO colloid solution then the mixture solution was thoroughly stirred for 30 min at room temperature. Boron content was controlled by adjusting mass ratio of Boron/(Boron+Carbon) (2.5, 5, 20%). After that, the solution was transferred into a 200 mL Teflon-lined stainless steel autoclave for hydrothermal treatment at 180 °C for 16 h and then cooled to room temperature naturally. The precipitate was separated by centrifugation and washed several times with deionized water and absolute ethanol, respectively. Obtained BGs were dried in a vacuum oven at 60 °C overnight. Herein, three BG samples with boron content of 1.23, 2.01, and 2.87 at%, as determined by X-ray photoelectron spectroscopy (XPS), were denoted as B_1G, B_2G, and B_3G, respectively (Table 1). For comparison, reduced graphene oxide (rGO, graphene) was synthesized under the same hydrothermal condition in the absence of $NaBH_4$ and was denoted as G. Round-shaped BG (or graphene) sheets were fabricated by vacuum filtration of BG (or G) colloid dispersion with DMF as solvent and further used to synthesize PN-BG (or PN-G) sheet.

2.1.2 Preparation of PN electrode. Polynitrogen N_8^- electrode synthesis was performed by CV treatment with a three-electrode setup followed our previous work [11] except using BG (or graphene) as substrates. BG (or graphene) ink was prepared with 10 mg BG (or graphene) powder ultrasonically dispersed into 5mL DMF containing a Nafion solution (0.5 wt%, DuPont). 5μL of the ink was coated onto the surface of a pre-polished glassy carbon electrode (GCE, 3.0 mm) denoted as BG-GCE (or G-GCE) and dried in air.

Then GCE was dipped in 40mL 2M NaN_3 (Aldrich)-buffer solution (PH=4.0), which was used as the working electrode. Pt and Ag/AgCl were used as counter and reference electrode, respectively. Herein, the different boron doping content samples are denoted as PN-B_1G, PN- B_2G, and PN-B_3G respectively. The resulting PN-BG-GCE and PN-G-GCE electrodes were dried in air and used as the working electrodes for ORR test.

PN-BG (or PN-G) sheet were prepared under the same electrochemical conditions using round-shaped BG (or graphene) sheets as working electrode to produce large amount of PN sheet samples for following characterizations.

2.2. Characterization. X-ray photoelectron spectroscopy (XPS) measurements were performed on a Kratos Axis Ultra DLD multitechnique XPS. The binding energy for all samples was calibrated by reference C1s binding energy (284.8 eV). Raman spectroscopy was performed with a Thermo Scientific DXR Raman microscope. SEM was performed on a Hitachi S-3400N scanning electron microscope and TEM was performed on a Hitachi H7500 TEM. FTIR was carried out using a Nicolet ThermoElectron FTIR spectrometer combined with a MIRacle ATR platform assembly and a ZnSe plate, and denoted as ATR-FTIR. The specific surface areas of the graphene and BG were determined by N_2 adsorption/desorption at liquid nitrogen temperature using an AutoChem 2920 II (Micromeritics). Temperature programmed decomposition (TPD) was carried out using the AutoChem II 2920 system. Samples were heated in flowing helium from room temperature to 850 °C at a heating rate of 10 °C /min. The released species were monitored with an on-line mass spectrometer (QMS 200, Stanford Research Systems).

2.3. Electrochemical measurements. The electrochemical tests were carried out in a rotating disk electrode (RDE) setup (ALS Co., Ltd) using linear sweep voltammetry (LSV)

measurements. For LSV measurements, the scanning rate is 5mV/s with various rotating speeds. PN-G-GCE and PN-BG-GCE electrodes were dried in air and used as working electrode directly. Pt and Ag/AgCl were used as the counter electrode and reference electrode, respectively. 0.1M KOH solution was used as electrolyte. Prior to the experiments, oxygen or nitrogen was bubbled into the electrolyte for at least 30 minutes until saturated; during the experiments, oxygen or nitrogen was flowed over the electrolyte to maintain saturation.

3. Results and discussion

3.1. Characterization of BG. The boron content and boron-bonding configuration in the graphene matrix were confirmed by XPS. The atomic percentages of boron in three boron-doped graphene samples (B_1G, B_2G and B_3G) were 1.23%, 2.01%, and 2.87%, respectively (Table 1). The boron doping content increased as the initial mass ration of $NaBH_4$ to GO dispersion increased.

Table 1. Parameters derived from XPS, BET, and Raman spectra measurements

Sample	Mass ratio of boron /Carbon	Boron content measured by XPS	BET	Raman
		B (wt.%)	(m^2/g)	I_D/I_G
Graphene	0	-	150.5	1.19
B_1G	2.5	1.23	131.1	1.26
B_2G	5	2.01	108.3	1.35
B_3G	20	2.78	72.8	1.48

The high-resolution XPS spectra of B1s, C1s for BG samples were performed and displayed in Figure 1 (The sample B_1G was taken as an example.). The higher B1s binding energy (192.1 eV) of B_1G, compared with that of pure boron (187.0 eV), suggesting that the boron atoms partially bonded to carbon atoms in sp^2-C network [21]. Moreover, the B1s peak could be fitted into two peaks at 192.0 eV and 192.4 eV, corresponding to BC_2O and BCO_2, respectively. The presence of BC_2O and BCO_2 bonds indicated boron atoms to replace carbon ones within graphene network and boron atoms doped at the defect sites, respectively. In addition, two new peaks at 284.7 eV and 286.6 eV were observed on the C1s spectrum of B_1G with comparison of graphene, which could be attributed to the presence of C-B_1 and C-B_2 [30, 31], respectively, indicating that boron atoms were bonded to carbon atoms in two types, which was in good agreement with the results of B1s. All of the above results demonstrated that boron atoms were successfully doped into the graphene matrix during the hydrothermal process.

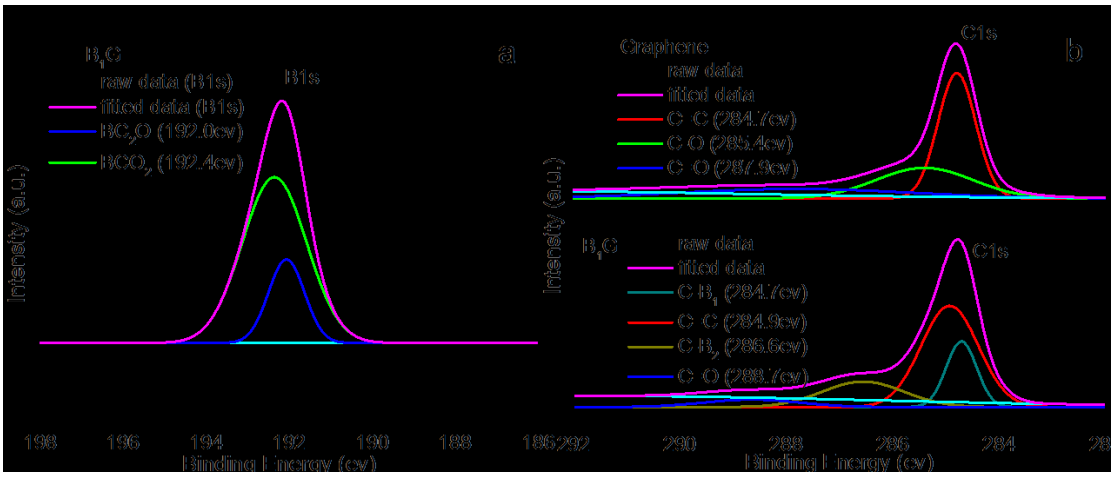

Figure 1. (a) B1s XPS spectra for boron-doped graphene; (b) C1s XPS spectra for graphene and boron-doped graphene.

Raman spectroscopy was carried out to characterize the quality of boron-doped graphene samples. The results were displayed in Figure 2. Two typical peaks, the D-band at ~ 1340 cm^{-1} and G-band at ~1570 cm^{-1}, were observed on all samples. The D-band (disordered band) indicated the structure defects while the G band was attributed to the E_{2g} phonon of sp^2-bonded graphitic carbons. The intensity ratio between the D and G bands (I_D/I_G) was commonly used to evaluate the defect level in graphene [32, 33]. As can be seen from Table 1, BG samples had larger I_D/I_G values (1.26-1.48) than that of graphene (1.19), indicating that the BGs possess many more defects than the graphene prepared under similar hydrothermal conditions due to boron doping. Furthermore, the increase of I_D/I_G ratio with the boron addition increase may suggest an increase in structural defects due to more boron doping into the graphene matrix in consideration of the same hydrothermal condition used.

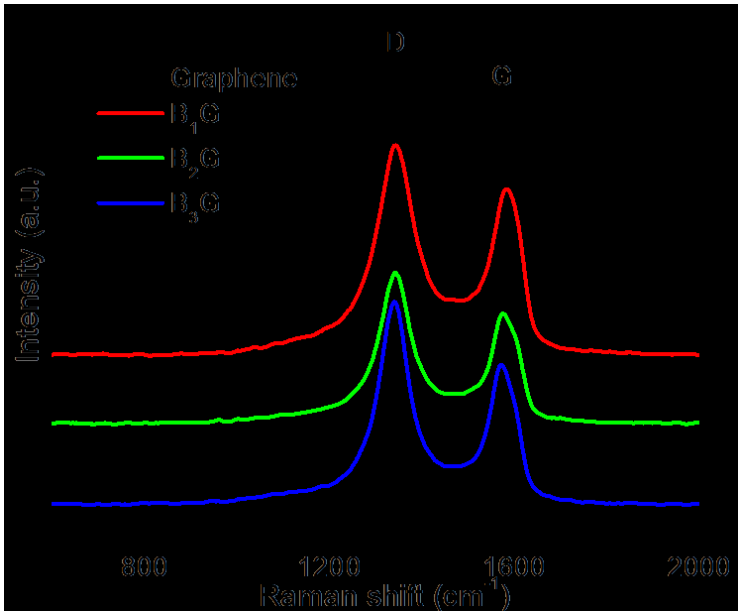

Figure 2. Raman spectra for graphene and boron-doped graphene.

The BET surface area data of different samples were also listed in Table 1. Graphene had a BET surface area of 150.6 m^2/g, which is much lower than the theoretical value. It could be attributed to the random agglomeration or restacking of the graphene layers during hydrothermal process [34]. The BET surface areas of B_1G, B_2G and B_3G were observed to be 131.1, 108.3, and 72.8m^2/g, respectively, suggesting that surface area of BG decreased with the increase of B content. In the case of high B content graphene, the introduction of B into the graphene network resulted in the recombination of some graphene layers comparing to the low boron content graphene case, and consequently decreased the BET surface area.

The morphology of graphene and BG were characterized by SEM and TEM. Similar to typical graphene structures (Figure S1(a) and (b)), B_1G nanosheets were randomly and loosely stacked together displaying white fungus structure (Figure 3(a)). Its TEM image (Figure 3(b)) showed the wrinkled graphene sheet with a low contrast under electron beam, indicating a small thickness of B_1G. B_1G with low boron doping content could well maintain graphene morphology. In contrast, B_3G nanosheets with high boron doping

content were compactly stacked together (Figure S1(c)) and their TEM images exhibited fragile and thick layers of graphene sheet (Figure S1(d)). It suggests that excessive amount of boron doping would destroy graphene structure, which may lead to the decrease of surface area and then disable the advantage of being a catalyst support. These structural images are consistent with aforementioned BET surface area data.

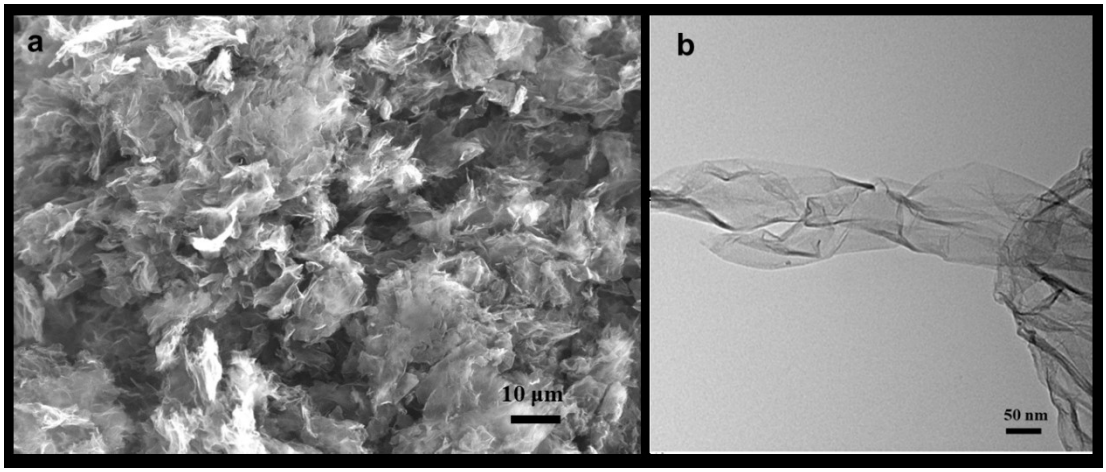

Figure 3. (a) SEM (b) TEM images of B_1G.

3.2. Characterization of PN-BG. The formation of PN on BG and graphene sheet after CV synthesis was confirmed by ATR-FTIR as shown in Figure 4a. The clear line at ~2050 cm^{-1} was the characteristic peak of N_8^- [11], suggesting that polynitrogen chain N_8^- was synthesized successfully. Moreover, the peak intensity, which corresponded to the synthesized N_8^- amount, followed the trend PN-B_1G > PN-B_2G > PN-G > PN-B_3G. The line near 2100 cm^{-1} was assigned to the azide ion asymmetric stretching mode from unreacted sodium azide [11]. The peak intensity, which corresponded to the residual N_3^- amount, followed the trend PN-B_3G > PN-G > PN-B_2G > PN-B_1G. The lines around 1560 cm^{-1}, 1390 cm^{-1} and 1200 cm^{-1} can be attributed to C=C of the graphene skeleton, C-OH

and epoxy C-O stretching vibrations respectively [35-37]. The lines around 1640 cm^{-1} and 3300 cm^{-1} were from residual water trapped in graphene sheet [11].

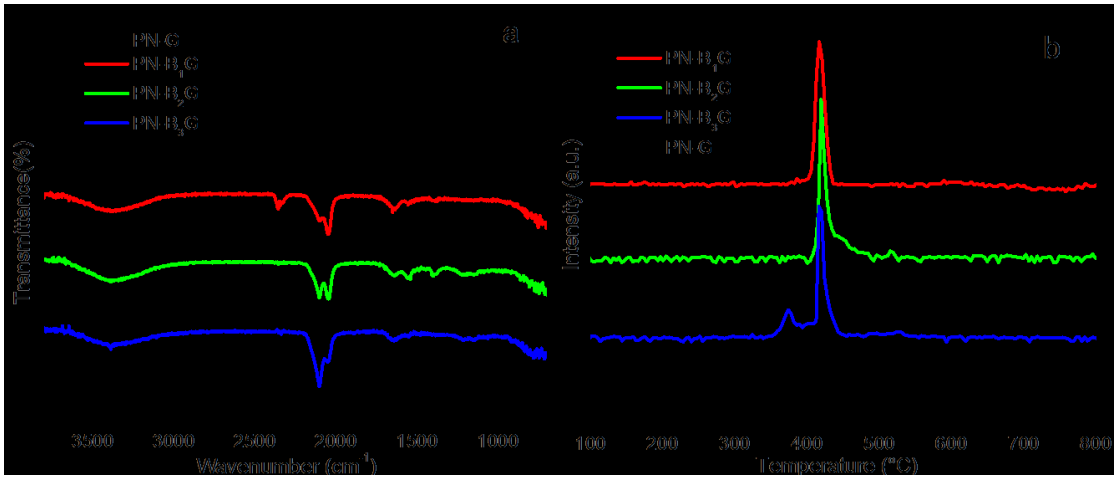

Figure 4. Characterization of PN-BG. (a) ATR-FTIR spectra. The graphene (boron-doped graphene) background was subtracted from the sample. (b) N^{14} signal from TPD scans. The curves were normalized by sample weight.

To investigate thermal stability of PN samples, TPD was carried out over different samples as shown in Figure 4b. The TPD scans showed that polynitrogen species N_8^- on graphene and BG substrates were thermally stable with decomposition temperature of 400 - 420 ºC. Moreover, desorption amount of nitrogen (Table 2) suggested that more N_8^- was synthesized on B_1G, while less N_8^- was observed on B_3G with trend of PN-B_1G > PN-B_2G > PN-G > PN-B_3G. Interestingly, two nitrogen desorption peaks were detected over PN-B_3G sample. The higher one corresponds to N_8^- stabilized on B_3G while the lower one can be attributed to azide deposited on B_3G. It was consistent with FTIR results, indicating that synthesis amount of N_8^- could be enhanced with the introduction of boron atoms in graphene network. Possibly, boron doping increased the electronegativity of carbon by electron clouds shifting from boron to carbon, which enhanced the charge transfer ability

from BG to the nitrogen chain and resulted into producing more PN on BG. However, in case of an excessive amount of boron doping, impurity scattering in the graphene lattice became more important. It led to the decrease in the conductivity [38, 39], which showed negative effects on the production of PN from azide during the electrochemical oxidation process [11]. Therefore, less N_8^- produced and more N_3^- would be residual on B_3G, which can be attributed to the too high boron doping content. Another reasonable explanation was from the different surface area of BG samples demonstrated by the BET, SEM and TEM. The active sites to stabilize PN chain were wrapped inside the graphene layers over B_3G sample with excessive boron content, which became inaccessible for PN stabilization. As a result, it led to lower amount of N_8^- synthesized. In contrast, the high surface area of B_1G exposed more active sites for PN chain stabilization, leading to a higher amount of N_8^-.

Table 2. Nitrogen desorption amount (mmol/grams of sample).

Entry	Sample	Nitrogen desorption amount[a]
1	PN-G sheet	1.00
2	PN-B_1G sheet	1.35
3	PN-B_2G sheet	1.11
4	PN-B_3G sheet	0.88

[a] calculated by integration of the TPD results and comparing the peak areas with those from injection of pure nitrogen under the same experiment conditions.

3.3. Electrocatalytic performance. To investigate the electrocatalytic performance of PN-G and PN-BG electrode, LSV was measured in an O_2-saturated 0.1 M KOH electrolyte using a rotating disk electrode (RDE) at a scan rate of $5mVs^{-1}$. The ORR polarization curves at different rotating speeds were shown in Figure 5a and Figure S2a-c. As expected, the catalytic current density of all samples increased with increasing the electrode rotating

speed due to the enhanced diffusion of electrolytes [40, 41]. Moreover, the current density followed the trend of PN-B_1G-GCE > PN- B_2G -GCE > PN-G-GCE > PN-B_3G-GCE at a certain potential (Figure 5c). This current density sequence was consistent with that of N_8^- amounts observed in FTIR and TPD. It prompted us to establish the relationship between ORR activity and the amount of N_8^- formed on graphene and BG substrates, which is consistent with our previous study. It proved that the larger amount of N_8^- deposited uniformly on MWNT substrate the more accessible active sites the PN-MWNT electrode could provide for dissolved oxygen to be reduced, leading to the electrocatalytic activity enhancement [11].

Kinetics of the ORR process was evaluated by the Koutecky-Levich (K-L) equation as following [42, 43]:

$$\frac{1}{J} = \frac{1}{J_L} + \frac{1}{J_k} = \frac{1}{B\omega^{0.5}} + \frac{1}{J_k} \qquad (1)$$

$$B = 0.62nFC_o(D_o)^{2/3}\nu^{-1/6} \qquad (2)$$

Where J is the measured current density, J_K and J_L are the kinetic and diffusion limiting current density, respectively. B is the Levich constant, n is the number of electrons transferred per oxygen molecule in the reaction, F is the Faraday constant (F=96485C cm^{-1}), C_o is the bulk concentration of O_2 (C_o=1.2×10^{-3}mol L^{-1}), D_o is the diffusion coefficient of O_2 (D_o=1.9×10^{-5} cm s^{-1}), ν is the kinematic viscosity of the electrolyte (ν=0.01cm^2 s^{-1}), ω is the angular velocity (rad s^{-1}). The Koutecky-Levich plots of 1/J vs. $1/\omega^{0.5}$ for all four samples were shown in Figure 5b and Figure S3a-c. The fitting lines for all samples were well-linear and parallel, which indicated a first-order reaction toward dissolved oxygen [44, 45]. Moreover, the electron transfer number n of different catalysts obtained from slopes of K-L plots were presented in Figure 5d. The n value at the PN-G-GCE electrode was derived

to be 3.7-3.8, which indicated that it was through a four-electron process over N_8^- [40, 44]. The similar n values (3.8-4.0, and 3.8-3.9) were achieved on PN-B_1G-GCE and PN-B_2G-GCE electrodes, respectively, which suggested that the pathways of both samples were also through a dominant four-electron process. However, the n value for PN-B_3G-GCE was 3.3-3.5, a number between two-electron and four-electron reduction processes, which suggested that the reaction may proceed by a coexisting pathway involving both the two-electron and four-electron transfers [46]. It can be attributed to the co-existence of N_3^- and N_8^- on PN-B_3G-GCE, ORR was a two-electron pathway on N_3^- (as discussed in following section) while followed a four-electron mechanism on N_8^-. To confirm the hypothesis, the electrocatalytic performance of several reference samples were further tested and illustrated in Figure S4a and S4b. Figure S4a showed an increased reduction current density in the order of PN-B_1G-GCE > PN- G-GCE > B_1G-GCE > NaN_3-B_1G-GCE > G-GCE. Clearly, the combination of PN and BG greatly enhanced the ORR performance. Moreover, electron transferred numbers (Figure S4b) of G-GCE, NaN_3-B_1G-GCE and B_1G-GCE were found to be 2.5-2.9, 2.6-3.0, and 3.4-3.7, respectively, in the potential range of -0.6V~-0.8V, which indicated the two-electron pathway over N_3^-.

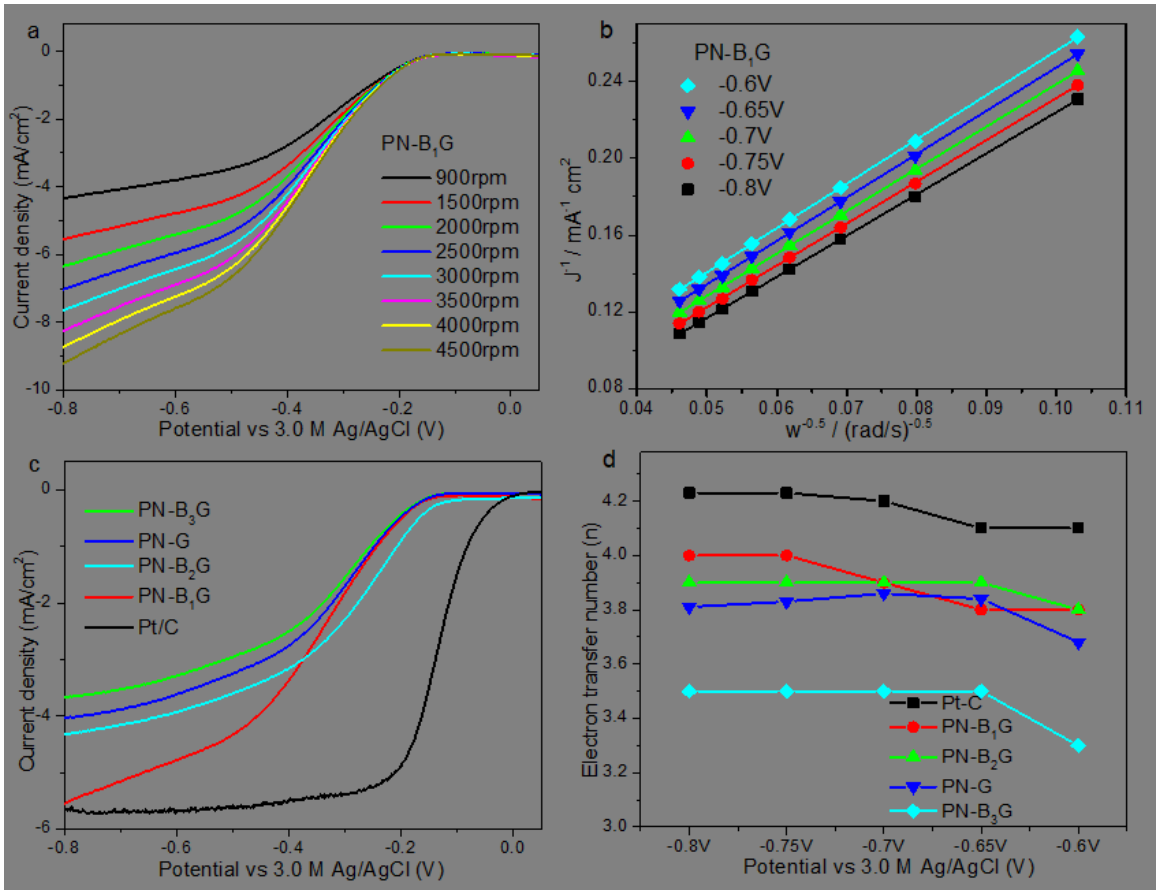

Figure 5. Electrocatalytic performance of PN-G and PN-BG samples. (a) LSV curves of PN-B_1G-GCE in an Oxygen-saturated 0.1 M KOH solution with different rotation speeds at scan rate of 5 mV/s. (b) K-L plots of PN-B_1G-GCE at different potentials. (c) LSV curves of PN-G-GCE, PN-B1G-GCE, PN-B2G-GCE， PN-B3G-GCE and Pt/C (10% platinum on Vulcan XC-72) in an Oxygen-saturated 0.1 M KOH solution with a rotation speed of 1500 rpm at scan rate of 5 mV/s. (d) Electron transfer number n of PN-G-GCE, PN-B1G-GCE, PN-B2G-GCE, PN-B3G-GCE and Pt/C (10% platinum on Vulcan XC-72) calculated from K-L equation.

The long-term stability of PN-B_1G and Pt/C catalysts were evaluated using a chronoamperometric method (Figure 6a). After 8000 s of reaction, the reduction current of

PN-B_1G exhibited a negligible decrease of ~1.5%, which is much better than that of the Pt/C catalyst (~14%).

For potential use in direct methanol fuel cells, methanol crossover effect of electrocatalyst should be tested. Herein, methanol tolerance abilities of PN-B_1G and Pt/C were investigated by injecting 0.5M methanol into an oxygen-saturated 0.1 M KOH solution during a chronoamperometric measurement. The results showed that reduction current of PN-B_1G didn't obviously decrease after the addition of 0.5M methanol, whereas the current from the commercial Pt/C decreased sharply (Figure 6b). This indicated that the methanol tolerance of PN-B_1G is superior to that of Pt/C.

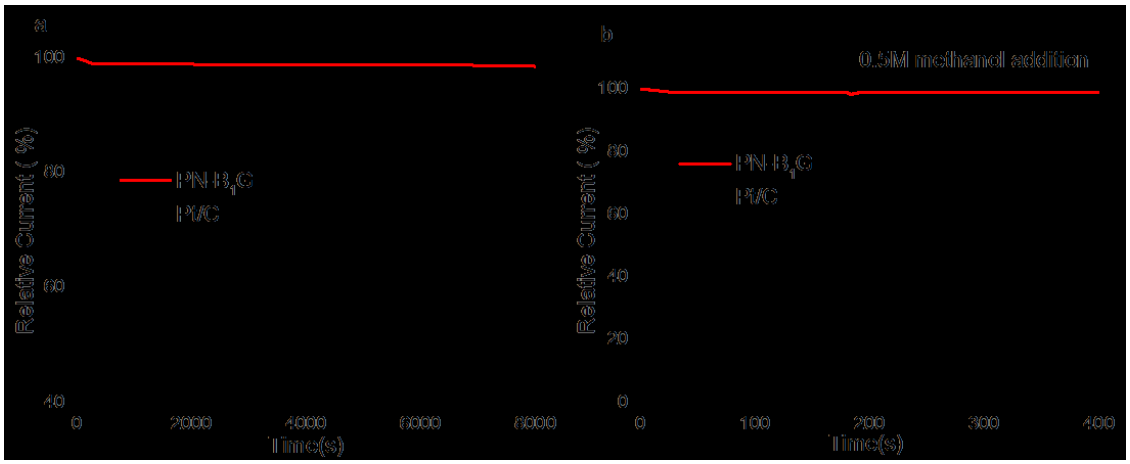

Figure 6. (a) Chronoamperometric curves of PN-B_1G and Pt/C in an Oxygen-saturated 0.1 M KOH solution with a rotation speed of 1500 rpm for 8000 s.

(b) Chronoamperometric curves of PN-B_1G and Pt/C in an Oxygen-saturated 0.1 M KOH solution with a rotation speed of 1500 rpm via the addition of 0.5M methanol was around 180s.

To clarify the oxygen reduction mechanism of PN over graphene and BG matrix, natural bonding orbital (NBO) analysis [11] was applied to investigate the chemisorption mode of O_2. Hirshberg et al. predicted that solid N_8 molecular crystal with chain structure is more

stable than other N_x polynitrogen based on DFT theoretical calculation [10]. Our previous study [11] further calculated the partial charge distribution on chain structure N_8^- species by NBO analysis. Based on the calculation results, the most active sites were N1 and N2 locating in the center of the chain with adjacent position because both had more negative charges than other nitrogen atoms (See Figure S5) where oxygen would tend to bondwith the electrons of N1 and N2 [11, 47]if the steric effect does not overrule the extra amount of negative charges, which will be clarified in our future work. Furthermore, the existence of the two adjacent active sites made it reasonable to propose that parallel diatomic adsorption (side-on adsorption, Yeager model [48]) onto N_8^- would serve as the dominant chemisorption mode of O_2 during ORR. Thus, the O-O bonding would be effectively weakened and easily broken by this side-on adsorption [49], which represented four-electron transfer pathway in ORR [50, 51]. Therefore, four-electron transfer pathway was observed in above kinetic study over N_8^-. On the other hand, N_3^- is a linear centrosymmetric anion with two end nitrogen atoms having more negative charges [52, 53], where the single site adsorption occurred and the ruling chemisorption mode of O_2 would be the end-on adsorption (Pauling model [48]). It would lead to a two-electron transfer pathway during ORR [50, 51], which is supported by the above kinetic study. The investigation of O_2 chemisorption mode on both N_8^- and N_3^- further confirmed the conclusion of the aforementioned kinetic study. The mechanism for oxygen reduction on N_3^- and N_8^- based on different O_2 chemisorption mode were illustrated in Figure 7.

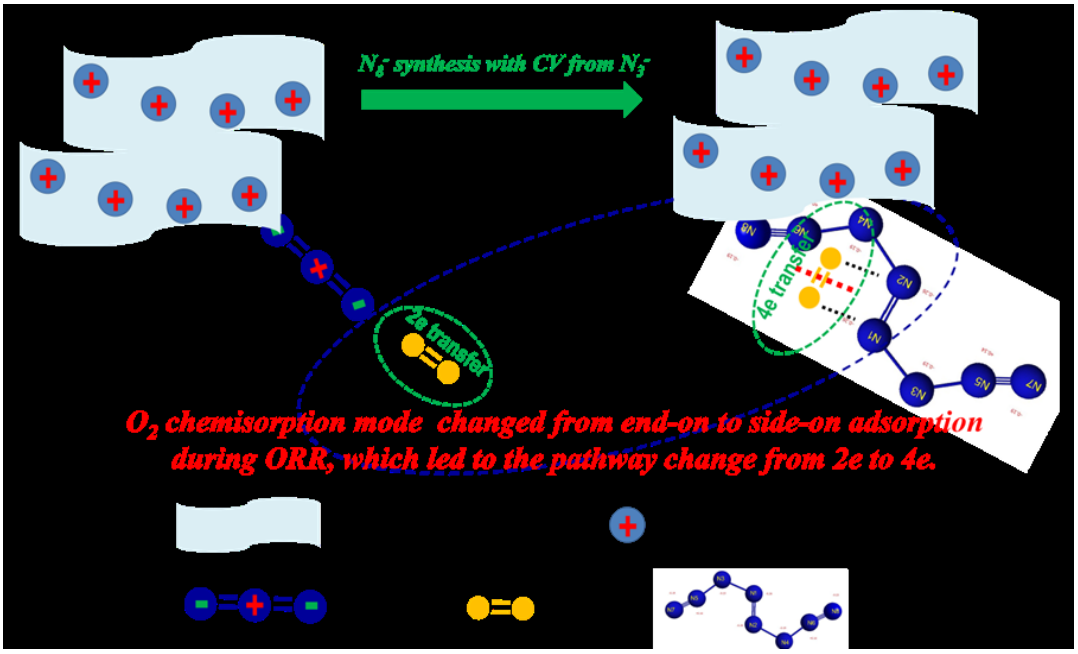

Figure 7. Schematic mechanism of high activity for ORR on N_3^- and N_8^- based on different O_2 chemisorption mode

4. Conclusion

Polynitrogen N_8^- (PN) deposited on boron-doped graphene (PN-BG) and graphene (PN-G) was synthesized experimentally for the first time by the cyclic voltammetry (CV) method under ambient condition. Boron-doped graphene (BG) were prepared by a facile hydrothermal method with the mixture of graphene oxide and $NaBH_4$. Compared to the graphene matrix, a larger amount of N_8^- was prepared on B_1G matrix. It was attributed to the boron doping, which enhanced the charge transfer ability from BG to PN chain resulting into producing more PN on BG. PN-BG and PN-G were further used as electrode catalysts for ORR, while the optimal former one (B_1G) showed the highest activity. It was ascribed to the larger amount of N_8^- observed on B_1G, which provided more active sites for ORR. Kinetic study revealed that it was through a four-electron process over N_8^-. It was further confirmed by O_2 chemisorption mode analysis, where the parallel diatomic adsorption

(side-on adsorption, Yeager model) was proposed. This work provides a facile strategy to modify graphene structure and efficiently stabilizes N_8^- on graphene based matrix for the first time.

ASSOCIATED CONTENT

AUTHOR INFORMATION

Corresponding Author

* E-mail: xianqin.wang@njit.edu

Author Contributions

#The authors contributed equally to this work.

Notes

The authors declare no competing financial interest.

Supporting Information

SEM and TEM images of graphene and B_3G, electrocatalytic performance of several BG and other reference samples, NBO partial charge distribution of N_8^- anion. The material is available free of charge via the Internet at http://pubs.acs.org.

Acknowledgements

This work was supported by NSF CBET-1804949.

References

(1) Uddin, J.; Barone, V.; Scuseria, G. E. Energy storage capacity of polymeric nitrogen. *Mol. Phys.* **2006,** 104, 745-749.

(2) Eremets, M. I.; Gavriliuk, A. G.; Trojan, I. A.; Dzivenko, D. A.; Boehler, R. Single-bonded cubic form of nitrogen. *Nat. Mater.* **2004,** 3, 558-563.

(3) Peng, F.; Yao, Y.; Liu, H.; Ma, Y. Crystalline LiN5 Predicted from First-Principles as a Possible High-Energy Material. *J. Phys. Chem. Lett.* **2015,** 6, 2363-2366.

(4) Wang, X.; Bao, K.; Tian, F.; Meng, X.; Chen, C.; Dong, B.; Li, D.; Liu, B.; Cui, T. Cubic gauche-CN: A superhard metallic compound predicted via first-principles calculations. *J. Chem. Phys.* **2010,** 133, 044512.

(5) Eremets, M. I.; Gavriliuk, A. G.; Serebryanaya, N. R.; Trojan, I. A.; Dzivenko, D. A.; Boehler, R.; Mao, H. K.; Hemley, R. J. Structural transformation of molecular nitrogen to a single-bonded atomic state at high pressures. *J. Chem. Phys.* **2004,** 121, 11296-11300.

(6) Tomasino, D.; Kim, M.; Smith, J.; Yoo, C.-S. Pressure-Induced Symmetry-Lowering Transition in Dense Nitrogen to Layered Polymeric Nitrogen (LP-N) with Colossal Raman Intensity. *Phys. Rev. Lett.* **2014,** 113, 205502.

(7) Plašienka, D.; Martoňák, R. Transformation pathways in high-pressure solid nitrogen: From molecular N2 to polymeric cg-N. *J. Chem. Phys.* **2015,** 142, 094505.

(8) Abou-Rachid, H.; Hu, A.; Timoshevskii, V.; Song, Y.; Lussier, L. S. Nanoscale high energetic materials: A polymeric nitrogen chain N8 confined inside a carbon nanotube. *Phys. Rev. Lett.* **2008,** 100(19), 196401.

(9) Ji, W.; Timoshevskii, V.; Guo, H.; Abou-Rachid, H.; Lussier, L. Thermal stability and formation barrier of a high-energetic material N 8 polymer nitrogen encapsulated in (5,5) carbon nanotube. *Appl. Phys. Lett.* **2009,** 95, 021904.

(10) Hirshberg, B.; Gerber, R. B.; Krylov, A. I. Calculations predict a stable molecular crystal of N8. *Nat. Chem.* **2014,** 6, 52-56.

(11) Wu, Z.; Benchafia, E. M.; Iqbal, Z.; Wang, X. N8 polynitrogen stabilized on multi-wall carbon nanotubes for oxygen-reduction reactions at ambient conditions. *Angew. Chem. Int. Ed.* **2014,** 53, 12555-12559.

(12) Shi, X.; Liu, B.; Liu, S.; Niu, S.; Liu, S.; Liu, R.; Liu, B. Polymeric Nitrogen A7 Layers Stabilized in the Confinement of a Multilayer BN Matrix at Ambient Conditions. *Sci. Rep.* **2018,** 8, 13758-13758.

(13) Niu, S.; Liu, S.; Liu, B.; Shi, X.; Liu, S.; Liu, R.; Yao, M.; Cui, T.; Liu, B. High energetic polymeric nitrogen sheet confined in a graphene matrix. *RSC Adv.* **2018,** 8, 30912-30918.

(14) Liu, S.; Yao, M.; Ma, F.; Liu, B.; Yao, Z.; Liu, R.; Cui, T.; Liu, B. High Energetic Polymeric Nitrogen Stabilized in the Confinement of Boron Nitride Nanotube at Ambient Conditions. *J. Phys. Chem. C* **2016,** 120, 16412-16417.

(15) Timoshevskii, V.; Ji, W.; Abou-Rachid, H.; Lussier, L. S.; Guo, H. Polymeric nitrogen in a graphene matrix: An ab initio study. *Phys. Rev. B: Condens. Matter Mater. Phys.* **2009,** 80, 115409.

(16) Geim, A. K.; Novoselov, K. S. The rise of graphene. *Nat. Mater.* **2007,** 6, 183-191.

(17) Chen, D.; Tang, L.; Li, J. Graphene-based materials in electrochemistry. *Chem. Soc. Rev.* **2010,** 39, 3157-3180.

(18) Seger, B.; Kamat, P. V. Electrocatalytically Active Graphene-Platinum Nanocomposites. Role of 2-D Carbon Support in PEM Fuel Cells. *J. Phys. Chem. C* **2009,** 113, 7990-7995.

(19) Hu, M.; Hui, K. S.; Hui, K. N. Role of graphene in MnO2/graphene composite for catalytic ozonation of gaseous toluene. *Chem. Eng. J.* **2014,** 254, 237-244.

(20) Hu, M.; Yao, Z.; Wang, X. Characterization techniques for graphene-based materials in catalysis. *AIMS Mater Sci.* **2017,** 4, 755-788.

(21) Bo, X.; Li, M.; Han, C.; Guo, L. The influence of boron dopant on the electrochemical properties of graphene as an electrode material and a support for Pt catalysts. *Electrochim. Acta* **2013,** 114, 582-589.

(22) Sun, Y.; Du, C.; An, M.; Du, L.; Tan, Q.; Liu, C.; Gao, Y.; Yin, G. Boron-doped graphene as promising support for platinum catalyst with superior activity towards the methanol electrooxidation reaction. *J. Power Sources* **2015,** 300, 245-253.

(23) Sun, Y.; Du, C.; Han, G.; Qu, Y.; Du, L.; Wang, Y.; Chen, G.; Gao, Y.; Yin, G. Boron, nitrogen co-doped graphene: a superior electrocatalyst support and enhancing mechanism for methanol electrooxidation. *Electrochim. Acta* **2016,** 212, 313-321.

(24) Varga, T.; Ballai, G.; Vásárhelyi, L.; Haspel, H.; Kukovecz, Á.; Kónya, Z. Co4N/nitrogen-doped graphene: A non-noble metal oxygen reduction electrocatalyst for alkaline fuel cells. *Appl. Catal., B* **2018,** 237, 826-834.

(25) Xu, Y.; Mo, Y.; Tian, J.; Wang, P.; Yu, H.; Yu, J. The synergistic effect of graphitic N and pyrrolic N for the enhanced photocatalytic performance of nitrogen-doped graphene/TiO2 nanocomposites. *Appl. Catal., B* **2016,** 181, 810-817.

(26) Hu, M.; Yao, Z.; Wang, X. Graphene-Based Nanomaterials for Catalysis. *Ind. Eng. Chem. Res.* **2017,** 56, 3477-3502.

(27) Hu, M.; Yao, Z.; Li, L.; Tsou, Y.-H.; Kuang, L.; Xu, X.; Zhang, W.; Wang, X. Boron-doped graphene nanosheet-supported Pt: a highly active and selective catalyst for low temperature H2-SCR. *Nanoscale* **2018,** 10, 10203-10212.

(28) Kovtyukhova, N. I.; Ollivier, P. J.; Martin, B. R.; Mallouk, T. E.; Chizhik, S. A.; Buzaneva, E. V.; Gorchinskiy, A. D. Layer-by-Layer Assembly of Ultrathin Composite Films from Micron-Sized Graphite Oxide Sheets and Polycations. *Chem. Mater.* **1999,** 11, 771-778.

(29) Li, H.; Liu, B.; Wang, Y.; Yin, S.; Ma, X.; Wang, X.; Wu, Q.; shen, R.; Chen, H. A facile one-step hydrothermal synthesis of a B-doped graphene/rod-shaped TiO2 nanocomposite. *RSC Adv.* **2014,** 4, 37992-37997.

(30) Yang, Y.; Zhang, J.; Wu, X.; Fu, Y.; Wu, H.; Guo, S. Composites of boron-doped carbon nanosheets and iron oxide nanoneedles: fabrication and lithium ion storage performance. *J. Mater. Chem. A* **2014,** 2, 9111-9117.

(31) Usachov, D. Y.; Fedorov, A. V.; Petukhov, A. E.; Vilkov, O. Y.; Rybkin, A. G.; Otrokov, M. M.; Arnau, A.; Chulkov, E. V.; Yashina, L. V.; Farjam, M.; Adamchuk, V. K.; Senkovskiy, B. V.; Laubschat, C.; Vyalikh, D. V. Epitaxial B-Graphene: Large-Scale Growth and Atomic Structure. *ACS Nano* **2015,** 9, 7314-7322.

(32) Zeng, X.; Wang, Z.; Meng, N.; McCarthy, D. T.; Deletic, A.; Pan, J.-h.; Zhang, X. Highly dispersed TiO2 nanocrystals and carbon dots on reduced graphene oxide: Ternary nanocomposites for accelerated photocatalytic water disinfection. *Appl. Catal., B* **2017,** 202, 33-41.

(33) Zhu, Y.; Cao, T.; Cao, C.; Luo, J.; Chen, W.; Zheng, L.; Dong, J.; Zhang, J.; Han, Y.; Li, Z.; Chen, C.; Peng, Q.; Wang, D.; Li, Y. One-Pot Pyrolysis to N-Doped Graphene with High-Density Pt Single Atomic Sites as Heterogeneous Catalyst for Alkene Hydrosilylation. *ACS Catal.* **2018,** 8, 10004-10011.

(34) Huang, C.; Li, C.; Shi, G. Graphene based catalysts. *Energy Environ. Sci.* **2012,** 5, 8848-8868.

(35) Guerrero-Contreras, J.; Caballero-Briones, F. Graphene oxide powders with different oxidation degree, prepared by synthesis variations of the Hummers method. *Mater. Chem. Phys.* **2015,** 153, 209-220.

(36) Nethravathi, C.; Rajamathi, M. Chemically modified graphene sheets produced by the solvothermal reduction of colloidal dispersions of graphite oxide. *Carbon* **2008,** 46, 1994-1998.

(37) Wang, Z. L.; Xu, D.; Huang, Y.; Wu, Z.; Wang, L. M.; Zhang, X. B. Facile, mild and fast thermal-decomposition reduction of graphene oxide in air and its application in high-performance lithium batteries. *Chem. Commun.* **2012,** 48, 976-978.

(38) Wei, D.; Liu, Y.; Wang, Y.; Zhang, H.; Huang, L.; Yu, G. Synthesis of N-Doped Graphene by Chemical Vapor Deposition and Its Electrical Properties. *Nano Lett.* **2009,** 9, 1752-1758.

(39) Humberto, T.; Ruitao, L.; Mauricio, T.; Mildred, S. D. The role of defects and doping in 2D graphene sheets and 1D nanoribbons. *Rep. Prog. Phys.* **2012,** 75, 062501.

(40) Jin, H.; Huang, H.; He, Y.; Feng, X.; Wang, S.; Dai, L.; Wang, J. Graphene Quantum Dots Supported by Graphene Nanoribbons with Ultrahigh Electrocatalytic Performance for Oxygen Reduction. *JACS* **2015,** 137, 7588-7591.

(41) Wang, W.; Chen, J.-Q.; Tao, Y.-R.; Zhu, S.-N.; Zhang, Y.-X.; Wu, X.-C. Flowerlike Ag-Supported Ce-Doped Mn3O4 Nanosheet Heterostructure for a Highly Efficient Oxygen Reduction Reaction: Roles of Metal Oxides in Ag Surface States. *ACS Catal.* **2019,** 9, 3498-3510.

(42) Lai, L.; Potts, J. R.; Zhan, D.; Wang, L.; Poh, C. K.; Tang, C.; Gong, H.; Shen, Z.; Lin, J.; Ruoff, R. S. Exploration of the active center structure of nitrogen-doped graphene-based catalysts for oxygen reduction reaction. *Energy Environ. Sci.* **2012,** 5, 7936-7942.

(43) Selvakumar, K.; Senthil Kumar, S. M.; Thangamuthu, R.; Ganesan, K.; Murugan, P.; Rajput, P.; Jha, S. N.; Bhattacharyya, D. Physiochemical Investigation of Shape-Designed MnO2 Nanostructures and Their Influence on Oxygen Reduction Reaction Activity in Alkaline Solution. *J. Phys. Chem. C* **2015,** 119, 6604-6618.

(44) Li, Y.; Zhao, Y.; Cheng, H.; Hu, Y.; Shi, G.; Dai, L.; Qu, L. Nitrogen-Doped Graphene Quantum Dots with Oxygen-Rich Functional Groups. *JACS* **2012,** 134, 15-18.

(45) Wang, Y.; Liu, H.; Wang, K.; Song, S.; Tsiakaras, P. 3D interconnected hierarchically porous N-doped carbon with NH3 activation for efficient oxygen reduction reaction. *Appl. Catal., B* **2017,** 210, 57-66.

(46) Wang, S.; Yu, D.; Dai, L. Polyelectrolyte Functionalized Carbon Nanotubes as Efficient Metal-free Electrocatalysts for Oxygen Reduction. *JACS* **2011,** 133, 5182-5185.

(47) Deng, D.; Pan, X.; Yu, L.; Cui, Y.; Jiang, Y.; Qi, J.; Li, W.-X.; Fu, Q.; Ma, X.; Xue, Q.; Sun, G.; Bao, X. Toward N-Doped Graphene via Solvothermal Synthesis. *Chem. Mater.* **2011,** 23, 1188-1193.

(48) Shi, Z.; Zhang, J.; Liu, Z.-S.; Wang, H.; Wilkinson, D. P. Current status of ab initio quantum chemistry study for oxygen electroreduction on fuel cell catalysts. *Electrochim. Acta* **2006,** 51, 1905-1916.

(49) Gong, K.; Du, F.; Xia, Z.; Durstock, M.; Dai, L. Nitrogen-Doped Carbon Nanotube Arrays with High Electrocatalytic Activity for Oxygen Reduction. *Science* **2009,** 323, 760-764.

(50) Zhang, L.; Xia, Z. Mechanisms of Oxygen Reduction Reaction on Nitrogen-Doped Graphene for Fuel Cells. *J. Phys. Chem. C* **2011,** 115, 11170-11176.

(51) Chen, R.; Li, H.; Chu, D.; Wang, G. Unraveling Oxygen Reduction Reaction Mechanisms on Carbon-Supported Fe-Phthalocyanine and Co-Phthalocyanine Catalysts in Alkaline Solutions. *J. Phys. Chem. C* **2009,** 113, 20689-20697.

(52) Stevens, E. D.; Hope, H. A study of the electron-density distribution in sodium azide, NaN3. *Acta Crystallogr., Sect. A* **1977,** 33, 723-729.

(53) Wang, X.; Li, J.; Zhu, H.; Chen, L.; Lin, H. Polymerization of nitrogen in cesium azide under modest pressure. *J. Chem. Phys.* **2014,** 141, 044717.

Table of Contents (TOC)